Springer

Acta Mechanica Sinica

CrossMark click for updates

• RESEARCH PAPER •

Acta Mech. Sin., Vol. 40, 723405 (2024)
https://doi.org/10.1007/s10409-023-23405-x

Temperature fluctuations and heat transport in partitioned supergravitational thermal turbulence

Dongpu Wang[1,2], Jing Liu[2], Rushi Lai[2], and Chao Sun[2,3*]

[1] *Beijing Key Laboratory of Space Thermal Control Technology, Beijing Institute of Spacecraft System Engineering, Beijing 100094, China;*
[2] *Center for Combustion Energy, Key Laboratory for Thermal Science and Power Engineering of MoE, and Department of Energy and Power Engineering, Tsinghua University, Beijing 100084, China;*
[3] *Department of Engineering Mechanics, School of Aerospace Engineering, Tsinghua University, Beijing 100084, China*

Received August 25, 2023; accepted October 31, 2023; published online January 18, 2024

We report an experimental study of the local temperature fluctuations δT and heat transport in a partitioned supergravitational turbulent convection system. Due to the dynamics of zonal flow in the normal system without partition walls, the probability density function (PDF) at a position in the mixing zone exhibits a downward bending shape, suggesting that the multi-plume clustering effect plays an important role. In partitioned system, zonal flow is suppressed and the PDFs indicate that the single-plume effect is dominant. Moreover, statistical analysis shows that the PDF of δT is sensitive to supergravity. Additionally, the thermal spectra follow $P(f) \sim f^{-5}$ in the normal system, which is relevant to the zonal flow. The absolute value of the scaling exponent of $P(f)$ and the scaling range become small in the partitioned system, which provides another evidence for the influence of zonal flow on the energy cascade. Further, heat transfer enhancement is found in the partitioned system, which may result from zonal flow being restricted and then facilitating the radial movement of thermal plumes to the opposite conducting cylinder. This work may provide insights into the flow and heat transport control of some engineering and geophysical flows.

Partitioned turbulent convection, Supergravity, Probability density function, Power spectra, Heat transfer

Citation: D. Wang, J. Liu, R. Lai, and C. Sun, Temperature fluctuations and heat transport in partitioned supergravitational thermal turbulence, Acta Mech. Sin. **40**, 723405 (2024), https:// doi.org/10.1007/s10409-023-23405-x

1. Introduction

Turbulent convection is ubiquitous in nature and engineering settings. For example, the convection in the sun [1, 2], the current movement in the ocean [3,4], the circulation in the atmosphere [5-7], the convective turbulent flow in the pumped fluid loop of thermal control system [8], the convective flow in the high-pressure compressor of the aero engine [9, 10] are all turbulent thermal convection. Rayleigh-Bénard convection (RBC) is a classical model for studying turbulent convection [11-16], in which the flow is heated from below and cooled from above. In order to increase the buoyancy-driven strength, recently, Jiang et al. [17], Rouhi et al. [18], Wang et al. [19,20] have proposed a supergravitational system (annular centrifugal RBC, ACRBC), in which it is observed that the scaling relation between the dimensionless heat transport, Nusselt number Nu, and the dimensionless buoyancy-driven strength, Rayleigh number Ra transitions to $Nu \sim Ra^{0.4}$ as Ra is larger than 10^{11} [21].

In the preliminary work, it was found that the convection rolls revolve around the cell center in the rotating frame, which means zonal flow appears in ACRBC [19]. And the thermal spectra exhibit $P(f) \sim f^{-5}$ [22]. It is considered that the balance between the phase velocity of zonal flow and the turbulent velocity at the Rhines scale may result in the Rhines scaling ($P(f) \sim f^{-5}$) [23-25]. In this paper, eight partition walls are mounted on the top lid of the cell so the convection rolls are restricted to fixed azimuthal positions. The dynam-

*Corresponding author. E-mail address: chaosun@tsinghua.edu.cn (Chao Sun)
Executive Editor: Chaofeng Lv

ics of zonal flow do not exist in the partitioned system. What do the PDFs and spectra of temperature fluctuations compare in ACRBC with and without partition walls? Answering this question will be one of the objectives of the present study.

In addition, visualized by the experimental streak image and numerical flow field, it is revealed that there exist four pairs of convection rolls in the high *Ra* regime of ACRBC [21]. So eight partition walls are adopted to divide the azimuthal region into eight subcells, each subcell includes one large-scale calculation (LSC) roll. Further, the aspect ratio between the azimuthal length at the mid radius and the width of the flow region $\Gamma_{\parallel} = \pi(R_o + R_i)/L \approx 9.42$, so each subcell divided by the eight partition walls is similar to classical RBC ($\Gamma \approx 1$) with rectangular sidewalls. In recent studies of classical RBC, Wang et al. [26, 27] provide a theoretical framework that can obtain the contribution of turbulent background and thermal plumes on the PDF of turbulent fluctuations quantitatively. In ACRBC, the effect of thermal plumes and their intermittency need to be studied, and comparing the results with those in classical RBC is necessary. We use the theoretical framework provided by Wang et al. [26,27] to analyze the temperature fluctuations in the different regions of partitioned ACRBC quantitatively.

Heat transport efficiency is a core problem in the community of turbulent convection [11]. Bao et al. [28,29] and Chen et al. [30] found that inserting vertical partitions into the rectangular convection cell can enhance heat transport significantly. In their system, the aspect ratio $\Gamma = 5$, so the case with 4 partitioned walls is similar to our system. It is reported that the heat transport of the case with 4 partitioned walls is found to increase by 25.3% (about 10% in their numerical results) compared with the case with no partitions [28]. However, due to the heat-carrying fluid being reduced in the partitioned system, Chen et al. [31] found that by inserting four partition plates at the four corners, *Nu* is only about 60% of the value in the normal RBC. Additionally, as partitions are inserted near the sidewalls or plates in classical RBC, the pattern of the mean LSC may be modified, while no significant variation of the heat transport is observed [32,33]. In partitioned ACRBC, we found heat transport enhancement in the high *Ra* regime although the gaps between the partition walls and the conducting cylinders are much larger than the thickness of the thermal boundary layers (BLs). So inserting partition walls that are along the normal direction of the conducting wall may be an effective approach to enhance the heat transport in rapidly rotating turbulent convection.

The aim of this paper is to suppress the zonal flow and study the statistics of temperature fluctuations and heat transport in the high *Ra* regime ($Ra > 10^{11}$) of the partitioned system. The remainder of this paper is organized as follows. In Sect. 2, we give a brief description of the experimental setup and methods. The results are presented and discussed in Sect. 3. Finally, the work is summarized in Sect. 4.

2. Methods

2.1 Experimental setup and methods

The turbulent convection experiments are carried out in a cylindrical annulus with a heated outer cylinder and a cooled inner cylinder [17, 21, 22]. The radius of the outer cylinder and inner cylinder are $R_o = 240$ mm and $R_i = 120$ mm, respectively. The two cylinders are machined from a solid piece of copper to ensure absolute concentricity. The whole convective region with a height $H = 120$ mm is sandwiched by two polycarbonate plates. Thus, the radius ratio is $\eta = R_i/R_o = 0.5$, and the aspect ratio between the height and the width of the flow region is $\Gamma_{\perp} = H/L = 1$. To reduce the influence of surrounding temperature fluctuations and minimize heat leakage, the ACRBC cell is wrapped in a proportional integral derivative (PID)-controlled jacket of which the temperature is the same as the outer cylinder and the entire system is placed in a thermostat throughout the measurements. As schematically shown in Fig. 1(b), eight polycarbonate partition walls of 8 mm thickness are vertically inserted into the convection cell, equally spaced along the azimuthal direction of the annular region and parallel to the radius of the cylinders, thus dividing the ACRBC cell into eight equal-sized subcells. Note that there are gaps of width $d = 5$ mm between the partition walls and the other three walls (see Fig. 1(a)), allowing the subcells to communicate with each other. The radial distance of the gap is from the conducting wall ($R' = 0$) to a location $R' = 5/120 = 0.042$, which is much larger than the thermal BL thickness ($\delta_{\text{th}}/L \simeq 1/(2Nu) \simeq [0.00085, 0.0028]$) and at the inner boundary of the mixing zone ($0.04 \lesssim R' \lesssim 0.3$) [27]. The consideration for choosing the width of "$d = 5$ mm" results from two aspects. The partitions are used to restrict the dynamics of the zonal flow in this paper. If the gap width is smaller than the thermal BL thickness or at the same order, the analysis of the heat transport and the difference of the temperature fluctuations will be coupled by two aspects. If the gap width is larger than the mixing zone, the thermal plumes could move across the gap and then it is disabled to restrict the zonal flow.

Four rubber heaters (Omega, XFR8/15) connected in series are attached to the outer surface of the outer cylinder to provide constant and uniform heating. The temperature of the inner cylinder is regulated by passing cold water through its internal channels using three water-bath machines (Polyscience, AP45R-20-A12E) and an extra pump (Wilo, PB-H170EAH). Two types of thermistors, i.e., the normal ther-

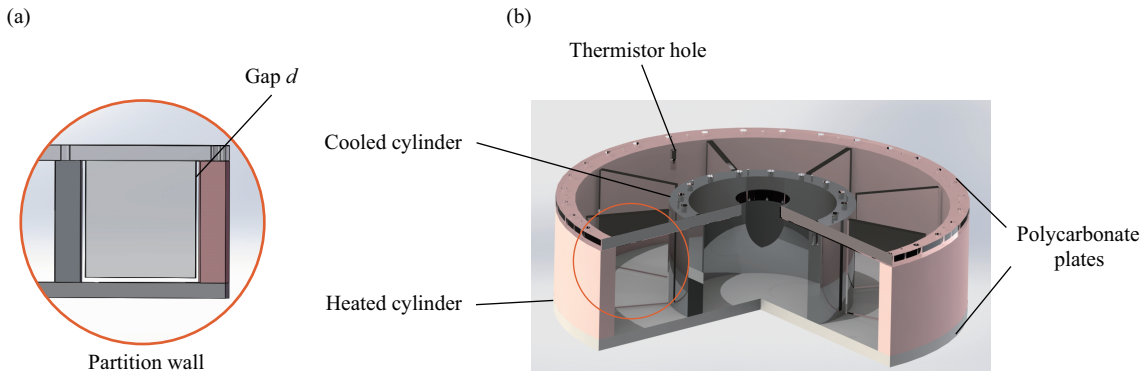

Figure 1 Sketch of the partitioned ACRBC cell with eight partition walls, dividing the whole azimuthal region into eight subcells. (a) Enlarged view of one partition wall. There are gaps of width $d = 5$ mm between the partition walls and the other three walls, allowing the subcells to communicate with each other. (b) The whole cell (only shows 2/3 azimuthal region).

mistors (Omega, 44031) and the fast-response thermistors (Amphenol, FP07DA103N), are used in our experiments. The temperature of the cylinders is monitored by nine normal thermistors which are embedded uniformly along the cylindrical walls. The response time of the normal thermistors is about 1 s. To measure the temperature fluctuations, two fast-response thermistors with smaller diameter ($\simeq 0.1$ mm) and ultra-fast response time of 7 ms are inserted into the flow through the thermistor holes at $R' \equiv (r - R_i)/L \simeq 0.2$ or $R' \simeq 0.5$ and $z = 0.5H$. The azimuthal positions of the two thermistors are, respectively, at the midpoint of the two partition walls and near one partition wall, and we refer to them as mid and side.

2.2 Parameter descriptions

Based on the dimensionless Boussinesq equations in the rotating reference frame, the flow is driven by the centrifugal buoyancy and affected by the Coriolis force. The dynamics of the flow are determined by the geometry of the cell and three dimensionless parameters. The first control parameter is the Rayleigh number, which reflects the buoyancy-driven strength:

$$Ra = \frac{1}{2}\omega^2(R_o + R_i)\alpha\Delta L^3/(\nu\kappa) \,. \tag{1}$$

The second is the Prandtl number, which reflects the ratio of momentum diffusivity to thermal diffusivity:

$$Pr = \nu/\kappa \,. \tag{2}$$

The last is the inverse Rossby number, which indicates the ratio of Coriolis force to inertial force:

$$Ro^{-1} = 2[\alpha\Delta(R_o + R_i)/(2L)]^{-\frac{1}{2}} \,. \tag{3}$$

Note that Coriolis effects can be alternatively reflected by the Ekman number, which is defined as

$$Ek = \nu/(2\omega L^2) \,. \tag{4}$$

Here, ω denotes the angular velocity of the system, $L = R_o - R_i$ is the width of the convective region in which R_o and R_i are the radius of the outer and inner cylinders, $\Delta = T_{\text{hot}} - T_{\text{cold}}$ is the temperature difference in which T_{hot} and T_{cold} are the temperature of the outer and inner cylinders. α, ν, and κ are the thermal expansion coefficient, kinematic viscosity, and thermal diffusivity, respectively. The working fluid adopts Novec-7200 (3M Inc. Engineered Fluid). For the physical properties of Novec-7200 fluid, we refer the reader to the supplementary materials of Jiang et al. [21]. By changing the temperature difference Δ and supergravity $sg \equiv \omega^2(R_o + R_i)/(2g)$, as shown in Table 1 of Appendix A, the Rayleigh number is varied over a range of $1.19\times10^{11} \le Ra \le 1.92\times10^{12}$. The range of inverse Rossby number is $8.97 \le Ro^{-1} \le 21.73$ and the Ekman number is in the range of $1.92\times10^{-7} \le Ek \le 6.43\times10^{-7}$. The Prandtl number $Pr \simeq 10$ and radius ratio $\eta = 0.5$ are fixed.

Heat transport is studied in the partitioned system. The global heat transport efficiency is reflected by the Nusselt number:

$$Nu = -JR_o \ln\eta/(\chi\Delta). \tag{5}$$

Here, $\eta = R_i/R_o$ is the radius ratio, J is the heat flux density through the outer cylinder into the system, and χ is the thermal conductivity. The definition of the Nusselt number in ACRBC is slightly different from that in classical RBC, which is due to the cylindrical geometry of the convection system [17]. In each case, the flow reaches a well-developed turbulence state after 6-8 h, and our measurement results are collected for at least 2 h after stabilization. A typical measurement of Nu lasts approximately 2-6 h (see Table 1 in Appendix A).

3. Results and discussion

3.1 PDFs in normal ACRBC

Firstly, let us discuss the results of experiments without partition walls. As the thermistor is located at $R' \simeq 0.2$, many cold plumes have just detached from the unstable thermal BL, while hot plumes have been probably diffused because of the turbulent dissipation. Based on the flow region defined in classical RBC [26, 27], the measured point is at the mixing zone ($0.04 \lesssim R' \lesssim 0.3$). We note that the BL thickness $\delta_{\text{th}}/L \simeq 1/(2Nu) \simeq 0.0017$ in the presently studied regime, so the measured point is far away from the BLs. As shown in Fig. 2(a), it is found that at $20g$ and $Ra \in [1.19\times10^{11}, 7.43\times10^{11}]$, the negative tail of the normalized temperature fluctuations $\delta T/\sigma_T$ has a large amplitude, which probably results from the contribution of cold plumes. Here, $\delta T = T(t) - \langle T\rangle_t$ is the temperature fluctuations measured by the thermistor inserted in the bulk flow, and σ_T is the root-mean-square (r.m.s.) value of $\delta T(t)$. He et al. [34] found that the effect of thermal plumes leads to the temperature fluctuation measured in the central region of the classical RBC exhibiting an exponential distribution:

$$P(\delta/\sigma) = \frac{1}{\sqrt{2}\sigma} \mathrm{e}^{-\sqrt{2}|\delta/\sigma|}, \tag{6}$$

which falls off much slower than a Gaussian function:

$$G(\delta/\sigma) = \frac{1}{\sqrt{2\pi}\sigma} \mathrm{e}^{-(\delta/\sigma)^2/2}. \tag{7}$$

While in the mixing zone of ACRBC, as shown in Fig. 2(a), the negative part of the PDF of $\delta T/\sigma_T$ exhibits a "downward-bending tail", which results in the decrease rate of PDF being even slower than the exponential distribution Eq. (6). The right-hand side of the peak in PDFs has a Gaussian-like shape (the black dashed line, Eq. (7)), which we believe results from the turbulent background. When the cold plumes form and are emitted into the mixing zone, they start to dominate the temperature fluctuations on the left-hand side of the peak in PDFs, which is highly non-Gaussian.

Recently, Wang et al. [27] have suggested a theoretical model including the multi-plume clustering/merging effect:

$$\begin{aligned} P(\delta/\sigma;\alpha_c,n_c,\beta_{sc},\beta_{mc}) = {} & \frac{(1-\beta_{sc}-\beta_{mc})\chi_1}{\sqrt{2\pi}} \exp\left\{-\frac{[\chi_1(\delta/\sigma)+\chi_2]^2}{2}\right\} \\ & + \frac{\beta_{sc}\alpha_c\chi_1}{2} \exp\left\{\frac{\alpha_c^2}{2} - \alpha_c[\chi_1(\delta/\sigma)+\chi_2]\right\} \operatorname{erfc}\left[\frac{\alpha_c-\chi_1(\delta/\sigma)-\chi_2}{\sqrt{2}}\right] \\ & + \frac{\beta_{mc}2^{(n_c-3)/2}\alpha_c^{n_c}\chi_1}{\sqrt{\pi}\Gamma(n_c)} \exp\left\{-\frac{[\chi_1(\delta/\sigma)+\chi_2]^2}{2}\right\}\left\{\Gamma\left(\frac{n_c}{2}\right)\cdot {}_1F_1\left[\frac{n_c}{2},\frac{1}{2},\frac{(\alpha_c-\chi_1(\delta/\sigma)-\chi_2)^2}{2}\right]\right. \\ & \left. + \sqrt{2}\Gamma\left(\frac{n_c+1}{2}\right)\cdot[\chi_1(\delta/\sigma)+\chi_2-\alpha_c]\cdot {}_1F_1\left[\frac{n_c+1}{2},\frac{3}{2},\frac{(\alpha_c-\chi_1(\delta/\sigma)-\chi_2)^2}{2}\right]\right\}. \end{aligned} \tag{8}$$

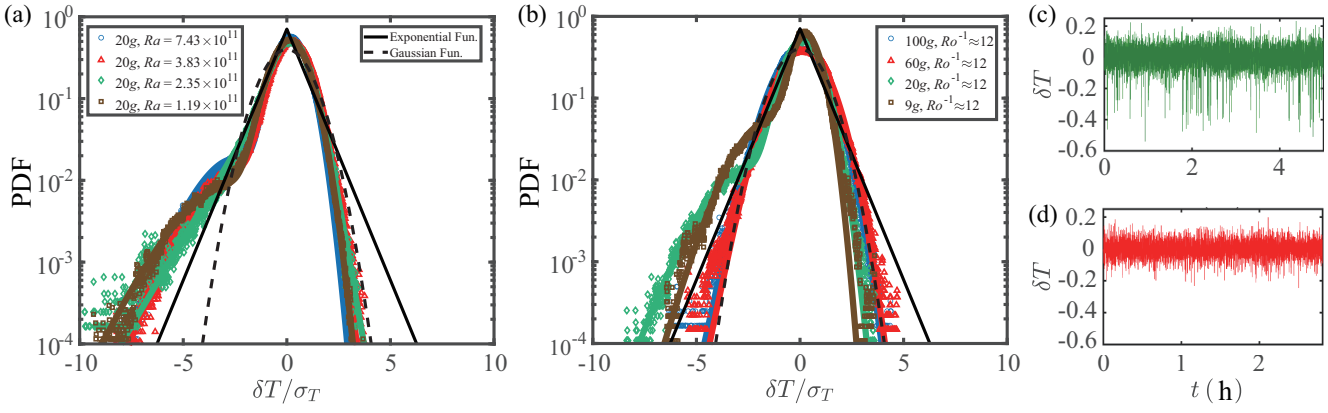

Figure 2 (a), (b) PDFs of the temperature fluctuations $\delta T/\sigma_T$ measured at $R' \simeq 0.2$ and $z = 0.5H$ in ACRBC without partition walls. For (a), the supergravity is fixed at $20g$ and Ra is varied by changing the temperature difference. For (b), Ro^{-1} is fixed at around 12, and Ra is varied by changing the supergravity. (c), (d) Time series of the temperature fluctuations δT at $20g$ and $60g$ for fixed $Ro^{-1} \simeq 12$. The black solid lines in (a) and (b) are the exponential function given in Eq. (6). The black dashed lines in (a) and (b) show the Gaussian function given in Eq. (7). The lines with the corresponding colors of the data points are the fits of the theoretical models proposed by Wang et al. [26, 27], and the fitting parameters are listed in Table 2 of Appendix B).

which includes the parameters $\alpha_c = \sigma_B/\sigma_c$, n_c, β_{sc}, and β_{mc}. Here, σ_B and σ_c are the r.m.s. values of the fluctuations contributed by turbulent background and cold plumes, respectively. n_c is the number of cold plumes. β_{sc} and β_{mc} characterize the spatial and temporal intermittency of the single-plume effect and the collective effect of multiple-cold plumes, respectively.

In the sidewall and outer BL regions of the classical RBC, the influence of multi-plume on temperature fluctuations is important. While in the mixing zone of classical RBC, the multi-plume effect can be neglected and the PDF exhibits an exponential-like long tail on one side because most thermal plumes are swept to the sidewall region by the LSC. So the PDF in the mixing zone of classical RBC is more approximate to the single-plume effect model [26]:

$$\begin{aligned} P(\delta/\sigma;\alpha_w,\alpha_c,\beta) = {} & \frac{(1-\beta)\gamma_2}{2}\exp[\alpha_c^2/2+\gamma_2(\delta/\sigma)+\beta\alpha_c/\alpha_w-1]\mathrm{erfc}\left[\frac{\alpha_c^2+\gamma_2(\delta/\sigma)+\beta\alpha_c/\alpha_w-1}{\sqrt{2}\alpha_c}\right] \\ & + \frac{\beta\alpha_w\gamma_2}{2(\alpha_w+\alpha_c)}\exp[\alpha_w^2/2-\gamma_1(\delta/\sigma)+\alpha_w/\alpha_c-\beta]\mathrm{erfc}\left[\frac{\alpha_w^2-\gamma_1(\delta/\sigma)+\alpha_w/\alpha_c-\beta}{\sqrt{2}\alpha_w}\right] \\ & + \frac{\beta\alpha_w\gamma_2}{2(\alpha_w+\alpha_c)}\exp[\alpha_c^2/2+\gamma_2(\delta/\sigma)+\beta\alpha_c/\alpha_w-1]\mathrm{erfc}\left[\frac{\alpha_c^2+\gamma_2(\delta/\sigma)+\beta\alpha_c/\alpha_w-1}{\sqrt{2}\alpha_c}\right], \end{aligned} \tag{9}$$

One additional parameters appear in Eq. (9), $\alpha_w = \sigma_B/\sigma_w$. Here, σ_w is the r.m.s. value of the fluctuations contributed by warm plumes. β in Eq. (9) corresponds to β_{sc} in Eq. (8).

In ACRBC, as shown in Fig. 2(a), it is found that the PDFs at $20g$ are more in agreement with the model involving the multi-plume effect, i.e., Eq. (8). The fitting parameters are listed in Table 2 of Appendix B. The error bar of the fitting parameters given in Table 2 of Appendix B represents the 95% confidence interval that we obtain from the fitting. It is found that the fitting parameter $\alpha_c \gtrsim 1$, which is similar to the case in the sidewall region of classical RBC. Meanwhile, the average number of plumes n_c in the multi-plume clusters is similar to that in classical RBC. The values of β_{sc} and β_{mc} are much smaller than that in classical RBC, suggesting that thermal plumes become more intermittent in time in ACRBC. In ACRBC, it is thought that the large number and strength of cold plumes at $R' \simeq 0.2$ are due to the dynamics of the zonal flow, which pushes the LSC rolls moving in a prograde/retrograde direction and leads to the cold plume triggering the spike-like signal [22]. In addition, the statistics in the mixing zone and the sidewall region cannot be distinguished clearly because of the existence of the azimuthal movement of zonal flow.

Further, considering the Coriolis force may affect the movement of plumes, we fix the effect of the Coriolis force ($Ro^{-1} \simeq 12$), and investigate the dependence of temperature fluctuations on supergravity. The measured time series of $\delta T/\sigma_T$ at $[8.9g, 20g]$ in the mixing zone (Fig. 2(c)) exhibits many large negative spikes, resulting in the negative part of PDF becoming relatively broad (Fig. 2(b)). This result suggests that cold plumes may be formed intermittently in the mixing zone. However, the number and amplitude of large negative spikes ($\delta T \lesssim -0.2$) decrease obviously at $[60g, 100g]$ (see Fig. 2(d)), and the PDF is more symmetric. The shape of the PDF of temperature fluctuations is more sensitive to the change of supergravity in the studied regime. The reason for the more symmetric shapes of the PDF may be due to the mixing effects of the LSC increasing significantly at higher centrifugal buoyancy, then the scale of plumes becoming smaller and the bulk flow becoming more homogeneous. The intermittency of plumes becomes small and the turbulent background contribution is large at $[60g, 100g]$, in Table 2 of Appendix B, it is seen that $\alpha_c \simeq 2.5$, which suggests the Gaussian-like turbulent background dominates the temperature fluctuations.

3.2 PDFs in partitioned ACRBC

Next, we examine the PDFs of temperature fluctuations obtained in partitioned ACRBC. The aim of adding partition walls is to restrict the dynamics of zonal flow. As shown in Fig. 3(c), the measured points are also at $R' \simeq 0.2$. The azimuthal position of one probe is at the midpoint of two partition walls, which is called by "mid point" in the following, and the other probe is near one partition wall, which is called by "side point" in the following.

It is observed that the downward-bending tail found in the PDF of normal ACRBC disappears in partitioned ACRBC (Fig. 3). The PDF is more like the results found in the mixing zone of classical RBC [26], in which the multi-plume effect is not important. A good agreement between the theory Eq. (9) and experimental results is obtained. At the midpoint and $20g$ (Fig. 3(a)), the PDFs are skewed toward the positive side and $\alpha_w < \alpha_c$ when $Ro^{-1} \in [9, 16]$, which in-

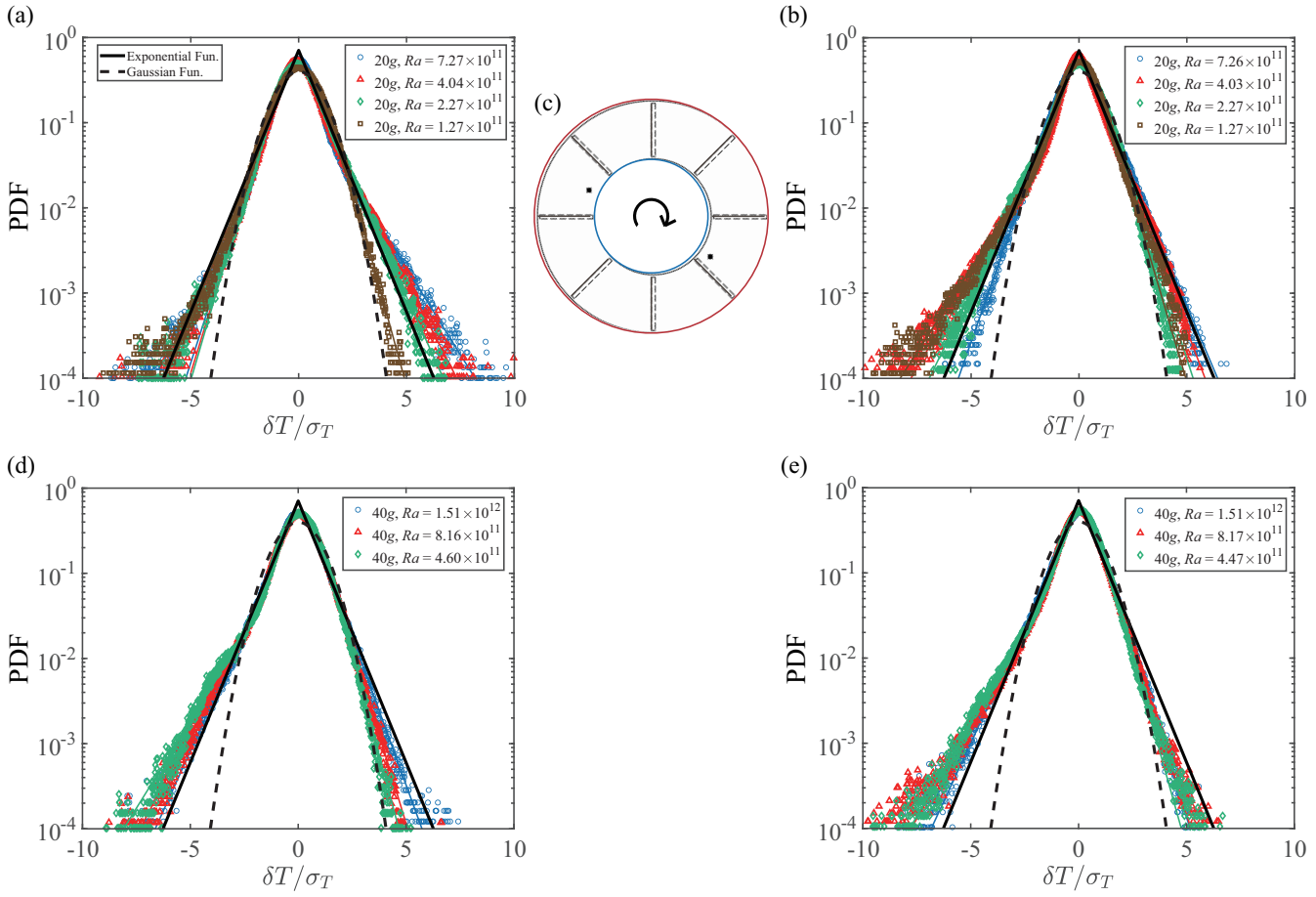

Figure 3 PDFs of the temperature fluctuations $\delta T/\sigma_T$ measured at $20g$ ((a), (b)) and $40g$ ((d), (e)) and different Ra at $z = 0.5H$. (c) Sketch of the top view of the cell shows that the radial positions of the two thermistors are both at $R' \simeq 0.2$, while the azimuthal positions are at the midpoint of the two partition walls and near one partition wall for (a), (d) and (b), (e), respectively. The arrow denotes that the system rotates clockwise for all cases. The black solid lines in (a) and (b) are the exponential function given in Eq. (6). The black dashed lines in (a) and (b) show the Gaussian function given in Eq. (7). The lines with the corresponding colors of the data points are the fits of the theoretical models proposed by Wang et al. [26, 27], and the fitting parameters are listed in Table 2 of Appendix B).

dicates some warm plumes can move to the region near the cold cylinder. Here, we should note that Ro^{-1} and Ra are negatively correlated as the supergravity and the fluid properties are fixed, for example, the largest Ro^{-1} case ($Ro^{-1} = 21.33$) corresponds to the smallest Ra case ($Ra = 1.27 \times 10^{11}$). With the increase of Ro^{-1}, the positive tail becomes small gradually. At $Ro^{-1} \simeq 21.33$, the PDF has been skewed toward the negative side. It is considered that the dependence of PDF on Ro^{-1} may be relevant to the influence of the Coriolis force and buoyancy force on the movement of plumes. At the side point and $20g$ (Fig. 3(b)), the PDFs are skewed toward the negative side and $\alpha_w > \alpha_c$ when $Ro^{-1} \in [12, 22]$, which indicates that cold plumes accumulate on the falling side of the LSC and produce many outward (negative) temperature fluctuations. With the increase of Ro^{-1}, the negative tail becomes large gradually. Both at mid and side points, the strength of cold plumes increases with the increase of Ro^{-1}.

At $40g$ (Fig. 3(d) and (e)), the PDFs are slightly skewed to the negative side both at the midpoint and side point. In addition, the measured PDFs for different values of Ro^{-1} and Ra at $40g$ are collapsed basically, especially for the PDFs measured at the side point (Fig. 3(e)), which illustrates the temperature fluctuations are not sensitive to the Coriolis force when the centrifugal buoyancy is large enough. The mixing effects of the LSC on the turbulent bulk region increase with increasing supergravity.

Given the obvious difference in the shape of PDFs between $20g$ and $40g$, we now discuss the dependence of PDFs of δT on supergravity at fixed $Ro^{-1} \simeq 12$. Figure 4(a) shows that at the midpoint, as the supergravity $sg \in [20g, 30g]$, the PDFs follow the exponential distribution Eq. (6) basically. The positive tail is slightly longer than the negative tail ($\alpha_c > \alpha_w$), which is the same as that in Fig. 3(a). As $sg \in [40g, 60g]$, the negative δT can still be described by the exponential function Eq. (6), while the positive δT follow Gaussian statistics Eq. (7) basically. The fitting parameters $\alpha_c < \alpha_w$ and α_w is larger than 1. It is thought that the increase of supergravity leads to the strong mixing effect of LSC, so warm plumes have been

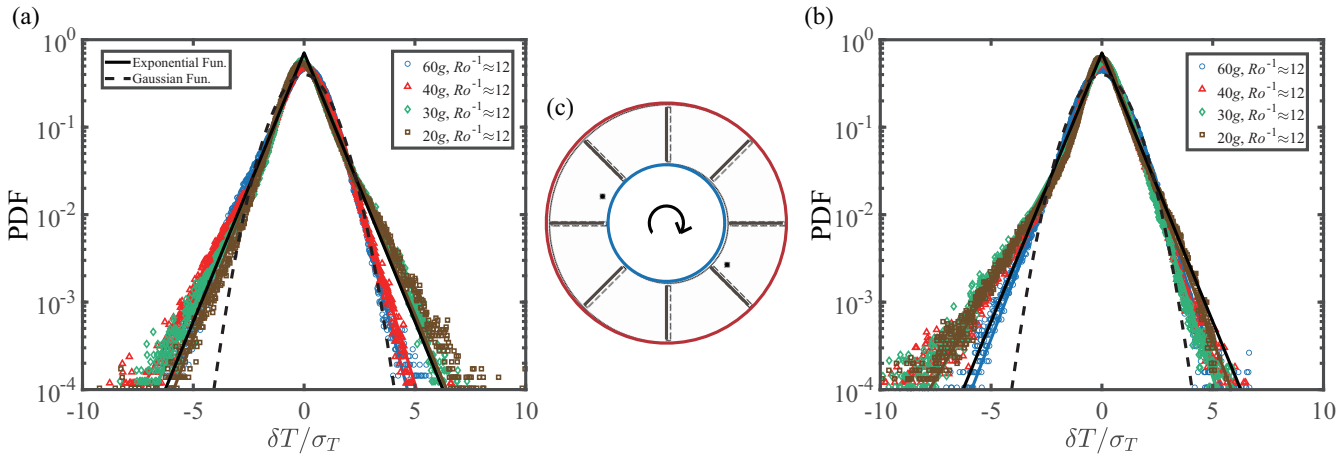

Figure 4 PDFs of the temperature fluctuations $\delta T/\sigma_T$ measured at $Ro^{-1} \simeq 12$ and different Ra at $z = 0.5H$. (c) Sketch of the top view of the cell shows that the radial positions are measured both at $R' \simeq 0.2$, while the azimuthal positions are at the midpoint of the two partitioned walls and near one partitioned wall for (a) and (b), respectively. The arrow denotes that the system rotates clockwise for all cases. The black solid lines in (a) and (b) are the exponential function given in Eq. (6). The black dashed lines in (a) and (b) show the Gaussian function given in Eq. (7). The lines with the corresponding colors of the data points are the fits of the theoretical models proposed by Wang et al. [26, 27], and the fitting parameters are listed in Table 2 of Appendix B).

diffused before reaching the region near the inner cylinder basically.

At the side point, as shown in Fig. 4(b), the positive tails are positioned between the standard Gaussian function Eq. (7) and the exponential function Eq. (6). The negative tails are larger than the exponential function Eq. (6). By comparing Fig. 4(a) with (b) and the corresponding fitting parameters, α_c at the side point is smaller than that at the midpoint, which demonstrates that the number and strength of cold plumes are larger at the side point than that at the midpoint at $R' \simeq 0.2$. We reveal that the reason may be due to the dynamics of the LSC roll. Similar to the classical RBC, most thermal plumes impact on the mid-region and eject near the sidewalls advected by the tilted elliptic LSC [35]. Note that at $60g$, the negative tail measured at the side point is slightly smaller than other cases and the PDF is symmetric basically, which may be due to the mixing effect of the LSC being stronger and the scale of thermal plumes being smaller with increasing Ra.

The PDFs of the temperature fluctuations are different obviously in different flow regions of classical RBC [26, 27]. In the mixing zone of classical RBC, one side of the PDFs follows the exponential function or Gaussian function, while the other side has an abrupt change in the local slope of the PDF, which is similar to the results in Fig. 4(b) of ACRBC. At the cell center of classical RBC, the asymmetry between the two exponential tails vanishes. However, in partitioned ACRBC, as R' moves towards the cell center ($R' \simeq 0.5$), it is found that the PDFs are skewed towards the negative side slightly (Fig. 5(a)) and the fitting parameters $\alpha_c < \alpha_w$ for all cases, which indicates that the number and strength of cold plumes are larger than those of warm plumes at the cell center. The reason for this asymmetric phenomenon may result from the asymmetric mean temperature field in ACRBC [19]. The bulk temperature is larger than the mean temperature, which gives rise to the cold plumes being stronger than the warm plumes. Moreover, the positive tails are positioned between the standard Gaussian function Eq. (7) and the exponential function Eq. (6), suggesting both the warm plumes and turbulent background contribute to the positive fluctuations.

Near the sidewalls and at the mid-radius of the ACRBC, one side of the PDFs follows the standard Gaussian function Eq. (7) well and the tails on the other side are larger than the exponential function Eq. (6) slightly (Fig. 5(b)), which is similar to the PDF measured in the mixing zone of classical RBC [26]. The large tails result from the single-plume effect advected by the LSC; the Gaussian statistics on the other side of the PDF are caused by the turbulent background fluctuation. We notice that the PDF of $\delta T/\sigma_T$ at $Ro^{-1} \simeq 21.7$ is different from the other three cases, which may be due to the change of the orientation of the LSC roll when the experiment restarts. Similar phenomena have been studied in classical RBC [36]. We have performed many experiments and found that the PDF measured near the sidewalls and at the mid-radius exhibits the two forms randomly. Note that the collective multi-plume effect is not important at the sidewall region of ACRBC. The model only including the single-plume intermittency can fit the PDFs well and $\beta_{sc} \simeq 0.3$, which is different from the PDF with a complex form measured near the sidewall of classical RBC [27].

3.3 Power spectra

In normal ACRBC, Figure 6(a) shows that the temperature frequency power spectra exhibit Rhines scaling $P(f) \sim f^{-5}$

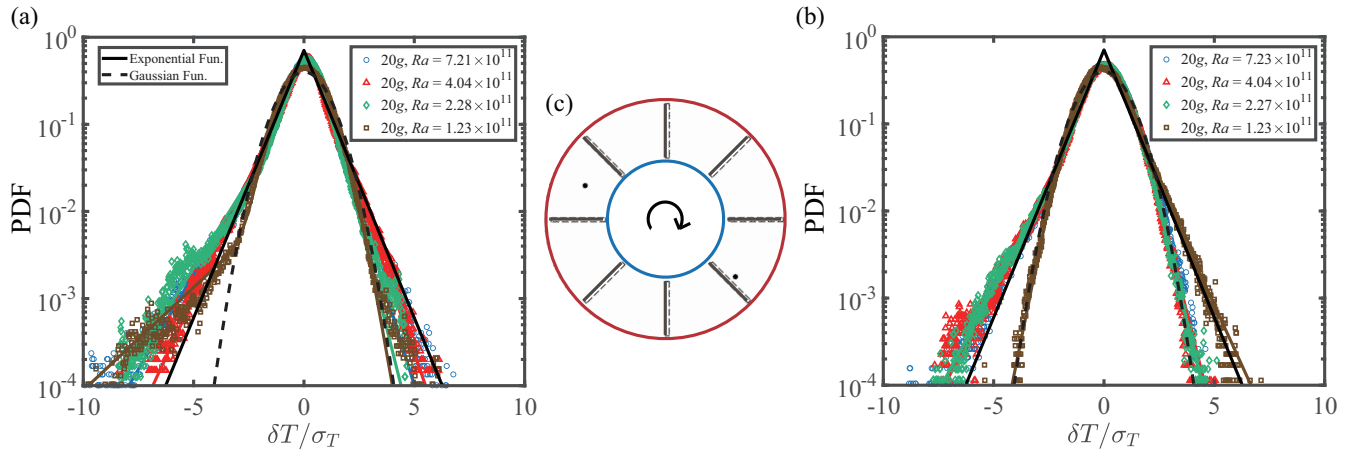

Figure 5 PDFs of the temperature fluctuations $\delta T/\sigma_T$ measured at $20g$ ((a), (b)) and different Ra at $z = 0.5H$. (c) Sketch of the top view of the cell shows that the radial positions are measured both at $R' \simeq 0.5$, while the azimuthal positions are at the midpoint of the two partitioned walls and near one partitioned wall for (a) and (b), respectively. The arrow denotes that the system rotates clockwise for all cases. The black solid lines in (a) and (b) are the exponential function given in Eq. (6). The black dashed lines in (a) and (b) show the Gaussian function given in Eq. (7). The lines with the corresponding colors of the data points are the fits of the theoretical models proposed by Wang et al. [26, 27], and the fitting parameters are listed in Table 2 of Appendix B).

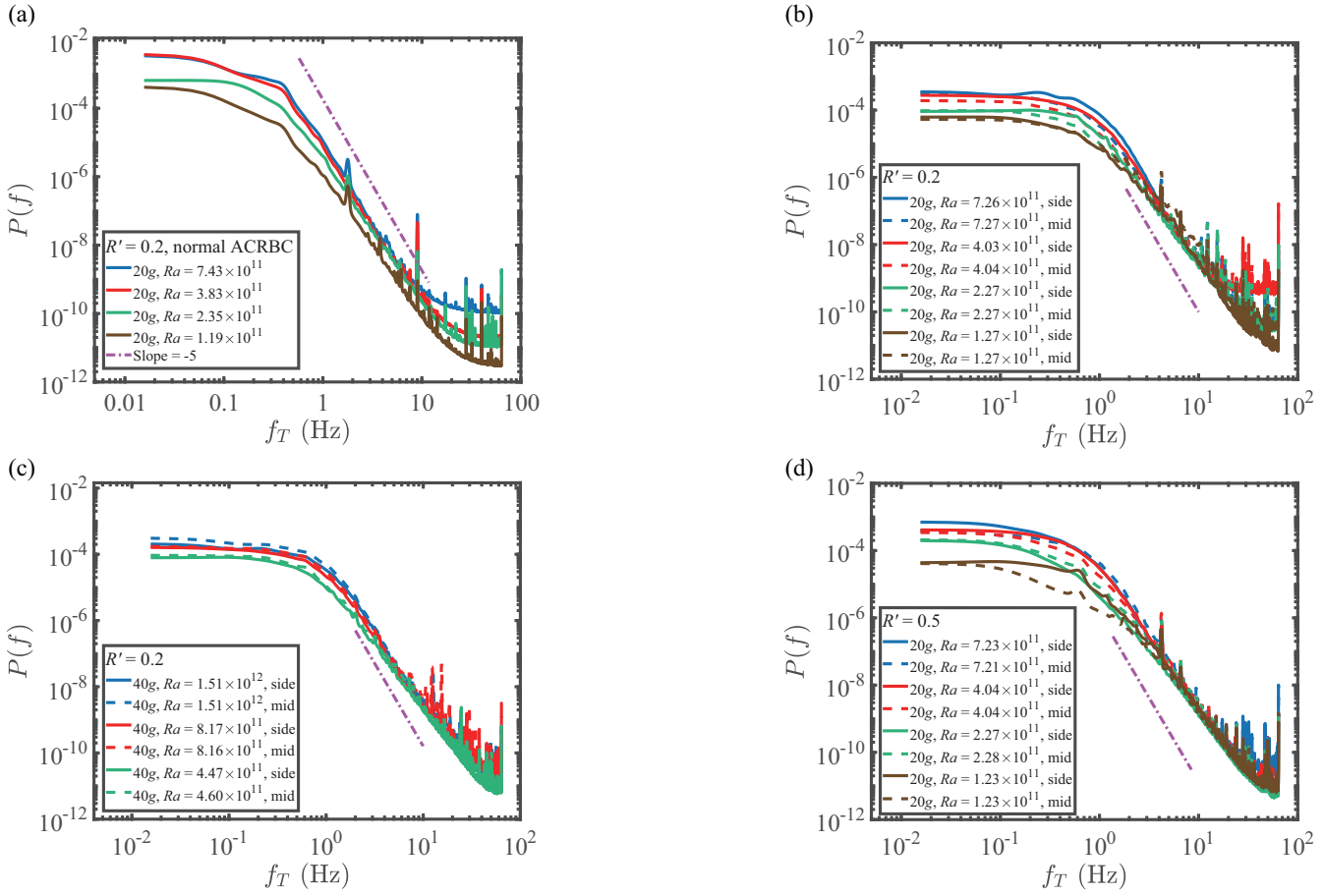

Figure 6 Power spectra of $\delta T(t)$. (a) $\delta T(t)$ are measured at $R' \simeq 0.2$ and $z = 0.5H$ in ACRBC without partition walls and the supergravity is fixed at $20g$. $\delta T(t)$ of (b) and (c) are measured at $R' \simeq 0.2$ and $z = 0.5H$ in partitioned ACRBC, while the supergravity is fixed at $20g$ and $40g$, respectively. (d) $\delta T(t)$ are measured at $R' \simeq 0.5$ and $z = 0.5H$ in partitioned ACRBC and the supergravity is fixed at $20g$. For (b)-(d), the solid lines correspond to $\delta T(t)$ measured at the side point and the dashed lines correspond to $\delta T(t)$ measured at the midpoint. The dash-dotted reference lines in (a)-(d) have a scaling of $P(f) \sim f^{-5}$.

over the range $0.4 \lesssim f \lesssim 10$ for different Ra and Ro^{-1}, implying the possible existence of inverse cascade due to turbulence in equilibrium with zonal flow [23-25]. In partitioned ACRBC, Fig. 6(b) and (c) shows the thermal spectra

measured at $R' \simeq 0.2$ (mixing zone) and $sg = 20g$, $40g$, respectively. Figure 6(d) shows the thermal spectra measured at $R' \simeq 0.5$ (cell center or near sidewall region) and $sg = 20g$. As shown in Fig. 6(b)-(d), it is found that the range of $P(f) \sim f^{-5}$ decreases obviously compared with the thermal spectra in normal ACRBC and the scaling of $P(f)$ over the range $3 \lesssim f \lesssim 20$ is not as steep as $P(f) \sim f^{-5}$ (the pink dash-dotted lines). This result provides further evidence for zonal flow leading to the Rhines scaling from an opposite perspective. Additionally, the absolute value of the scaling exponent decreases with the increase of Ro^{-1}.

In addition, in normal ACRBC, it is observed that the amplitude of the thermal spectra increases with the decrease of f over the range of $f \lesssim 0.4$, while the power spectra in partitioned ACRBC are flat in this range of frequency. We note that the time scale of zonal flow found in normal ACRBC is in this range, which is much larger than the time scale of the LSC and the inverse rotation rate [22]. The flat spectra at large scales in Fig. 6(b)-(d) suggest that zonal flows have been restricted and do not exist in partitioned ACRBC.

Further, it is found that the amplitude of the thermal spectra measured at the cell center is lower than that measured near the sidewalls basically (Fig. 6(d)), which suggests the LSC exists in the subcell of the partitioned ACRBC, resulting in the flow being strong near the sidewalls and relatively weak at the cell center. At $R' \simeq 0.2$, the result is slightly different for $20g$ and $40g$. At $20g$, the amplitude at the midpoint is lower than that at the side point (Fig. 6(b)), which suggests that the flow at the side point has more kinetic energy than that at the midpoint. While at $40g$, the amplitude at the midpoint is higher than that at the side point (Fig. 6(c)). The difference may be attributed to the strong mixing effect at high supergravity, which needs to be further studied.

3.4 Heat transport

In normal ACRBC, a possible ultimate scaling dependence of Nu on Ra has been observed at $Ra \gtrsim 10^{11}$ [21]. The dependence of Nu on Ro^{-1} is not obvious in the presently studied regime. In partitioned ACRBC, it is also found that Nu is basically independent on Ro^{-1}. So we use the same symbol (open upright triangle) to denote $Nu(Ra)$ measured in the partitioned system. Figure 7(a) shows that the scaling of $Nu(Ra)$ of partitioned ACRBC is similar to that in normal ACRBC, while the amplitude becomes larger. We note that in partitioned ACRBC, Nu is increased by approximately 6%-12%, which is larger than the experimental error. We have also reconducted four cases of normal ACRBC experiments (closed inverted triangle), and the experimental results confirm that the heat transfer of partitioned ACRBC is higher than that of normal ACRBC. In addition, we use the power function to fit the experimental data of partitioned ACRBC or normal ACRBC. In partitioned ACRBC, Nu and Ra obey a relation of $Nu = 0.0056 \times Ra^{0.41}$ for $Ra \geq 2 \times 10^{11}$. The scaling exponent 0.41 in partitioned ACRBC is similar to 0.40 found in normal ACRBC over the range of $5\times10^{10} \leq Ra \leq 5\times10^{12}$, which provides another evidence for the observation of Kraichnan-like ultimate regime [37-40] in ACRBC. We also note that in partitioned ACRBC, Nu at $Ra \simeq 1.25\times10^{11}$ (case 12, 16, 34, 38 in Table 1 of Appendix A) is approximate to Nu measured in normal ACRBC. On the one hand, as shown in Fig. 7(b), the increment of Nusselt number $\delta Nu = Nu_{\rm par} - Nu_n$ increases with increasing Ra slightly. So the difference of heat transport may be very small at relatively small Ra. On the other hand, the temperature difference of these four cases is small ($\Delta \simeq 3.5$K), so the temperature of the environment may have a relatively large influence on the measurement of heat transport.

For ACRBC with averaged aspect ratio $\Gamma_{\|} \simeq 9$, Nu with 8 partitioned walls is found to increase by about 10% at $Ra \simeq 10^{12}$ comparing with the cases with no partitions. In classical RBC with aspect ratio $\Gamma = 5$ and 4 partition walls, Bao et al. [28] found that the heat transport enhancement is also about 10% in their numerical results (see their Fig. 2). They considered that the strong horizontal jets in thin gaps are the main reason for the heat-transfer enhancement. The gap height of their system $d = 2$ mm is of the order of the thermal BL thickness $\delta_{\rm th} \simeq 2$ mm. So the sweeping effect of the jets on the BL is significant. While in our system, the gap $d = 5$ mm and $\delta_{\rm th} \simeq L/(2Nu) \simeq 0.2$ mm. The normalized gap height $d/\delta_{\rm th} \simeq 25$, so this factor may be not dominant. The effect of gap width on heat transport could be studied in further work.

We think that the heat transport enhancement may result from the suppression of zonal flow in partitioned ACRBC. In our previous numerical study (see Fig. 9 of Wang et al. [19]), we found that Nu at radius ratio $\eta = 0.5$ (the present experimental size) is approximately 90% of that at $\eta = 0.9$ which is similar to classical RBC and zonal flow is very weak. The thermal plumes (heat transfer carriers) can be swept away by the shear of zonal flow. So the restriction of zonal flow by the partition walls may enhance the heat transport.

4. Conclusion

We present a comparative experimental study of the temperature fluctuation and heat transport in ACRBC with or without partition walls. Firstly, in normal ACRBC, the negative side of the PDFs of $\delta T/\sigma_T$ at $R' \simeq 0.2$ has a downward-bending tail, which results from the multi-plume clustering effect according to the analysis of the theoretical model; at

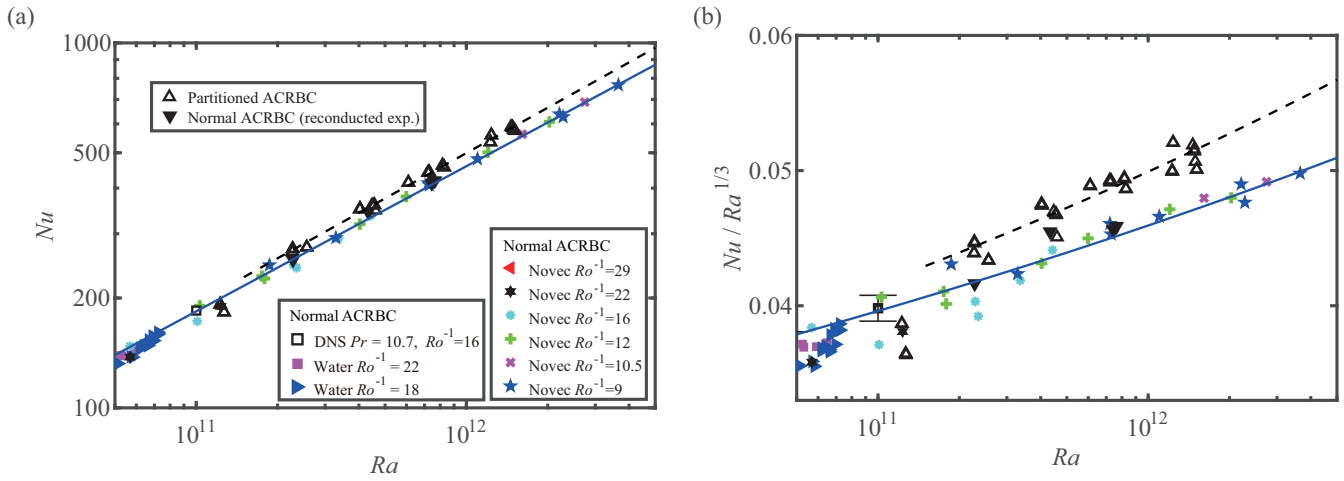

Figure 7 Global heat transport. (a) Nusselt number Nu as a function of Rayleigh number Ra, (b) the compensated plots of $Nu/Ra^{1/3}$ versus Ra. The open triangular symbols denote the results measured in partitioned ACRBC. Other symbols denote the results measured in normal ACBRC without partition walls [21]. The black dashed line is the power law that fits the data measured in partitioned ACRBC for $Ra \geq 2 \times 10^{11}$, which is $Nu = 0.0056 \times Ra^{0.41}$. The blue line is the power law that fits the data measured in normal ACRBC for $Ra \geq 5 \times 10^{10}$, which is $Nu = 0.0078 \times Ra^{0.40}$.

$R' \simeq 0.2$ of the partitioned ACRBC, the downward-bending tails disappear for all cases, which suggests the multi-plume effect is not important. The existence of zonal flow in normal ACRBC leads to the coupling of the statistics in the mixing zone where the single-plume effect is dominant and the sidewall region where the multi-plume effect cannot be neglected. In addition, the PDFs of temperature fluctuations are sensitive to supergravity. The mixing effect of the LSC is stronger at higher supergravity, leading to the flow becoming more homogeneous and the contribution of the turbulent background becoming larger.

Secondly, in normal ACRBC, because of the balance of zonal flow and turbulent fluctuation, the temperature power spectra exhibit Rhines scaling $P(f) \sim f^{-5}$ in nearly two decades of scales. The amplitude of spectra increases with the decrease of frequency at a small frequency, which demonstrates the existence of the zonal flow. In partitioned ACRBC, the absolute value of the scaling exponent of $P(f)$ is relatively small and the scaling range becomes no more than one decade of scales. The amplitude of spectra is independent of the frequency at a small frequency. Thus it is verified that $P(f) \sim f^{-5}$ found in normal ACRBC results from the dynamics of the zonal flow.

Thirdly, in normal ACRBC, the scaling exponent of $Nu(Ra)$ is 0.40 at $5 \times 10^{10} \lesssim Ra \lesssim 5 \times 10^{12}$; in partitioned ACRBC, the scaling exponent of Nu and Ra at $2 \times 10^{11} \lesssim Ra \lesssim 2 \times 10^{12}$ is 0.41, which provides another evidence for the achieving ultimate regime by strong centrifugal buoyancy in ACRBC. In addition, the amplitude of Nu is enhanced by about 10% compared with the cases of normal ACRBC, which may be due to the zonal flow being restricted and more thermal plumes reaching the opposite conducting plate. The magnitude of the heat transport enhancement in ACRBC adding partitions is similar to the result found in classical RBC. Thus inserting partition walls in the convection system is probably a universal method to enhance heat transport, which may give insights into some industrial applications.

Conflict of interest *On behalf of all authors, the corresponding author states that there is no conflict of interest.*

Author contributions *Chao Sun designed the research. Dongpu Wang and Jing Liu wrote the first draft of the manuscript. Dongpu Wang and Rushi Lai set up the experiment set-up and processed the experiment data. Chao Sun helped organize the manuscript. All authors revised and edited the final version.*

Acknowledgements *This work was supported by the National Natural Science Foundation of China (Grant No. 11988102), and the New Cornerstone Science Foundation through the XPLORER PRIZE. We thank Hongyang Zheng for the helpful discussions.*

1 S. M. Hanasoge, H. Hotta, and K. R. Sreenivasan, Turbulence in the Sun is suppressed on large scales and confined to equatorial regions, Sci. Adv. **6**, eaba9639 (2020).
2 J. Schumacher, and K. R. Sreenivasan, Colloquium: Unusual dynamics of convection in the Sun, Rev. Mod. Phys. **92**, 041001 (2020).
3 L. Cheng, J. Abraham, Z. Hausfather, and K. E. Trenberth, How fast are the oceans warming? Science **363**, 128 (2019).
4 Y. Yang, Double diffusive convection in the finger regime for different Prandtl and Schmidt numbers, Acta Mech. Sin. **36**, 797 (2020).
5 Y. D. Afanasyev, and Y. Zhang, Cyclonic circulation of Saturn's atmosphere due to tilted convection, Nat. Geosci **11**, 164 (2018).
6 X. Tan, M. Lefévre, and R. T. Pierrehumbert, Convection modeling of pure-steam atmospheres, Astrophys. J. Lett. **923**, L15 (2021), arXiv: 2111.15265.
7 B. Zhang, Y. Xiang, S. Xue, K. Zheng, Q. Zhong, and Y. Zhang, Analysis of the influence of Mars surface thermal environment on spacecraft thermal control (in Chinese), Chin. Space Sci. Technol. **41**, 55 (2021).
8 Q. Liu, C. Yang, K. Xu, and X. Zhao, Design and simulation of two-phase thermal control system for space high power source (in Chinese),

Chin. Space Sci. Technol. **43**, 104 (2023).
9 D. Bohn, E. Deuker, R. Emunds, and V. Gorzelitz, Experimental and theoretical investigations of heat transfer in closed gas-filled rotating annuli, J. Turbomach. **117**, 175 (1995).
10 J. Michael Owen, and C. A. Long, Review of buoyancy-induced flow in rotating cavities, J. Turbomach. **137**, (2015).
11 G. Ahlers, S. Grossmann, and D. Lohse, Heat transfer and large scale dynamics in turbulent Rayleigh-Bénard convection, Rev. Mod. Phys. **81**, 503 (2009), arXiv: 0811.0471.
12 F. Chillá, and J. Schumacher, New perspectives in turbulent Rayleigh-Bénard convection, Eur. Phys. J. E **35**, 58 (2012).
13 D. Lohse, and K. Q. Xia, Small-scale properties of turbulent Rayleigh-Bénard convection, Annu. Rev. Fluid Mech. **42**, 335 (2010).
14 M. K. Verma, A. Kumar, and A. Pandey, Phenomenology of buoyancy-driven turbulence: Recent results, New J. Phys. **19**, 025012 (2017), arXiv: 1611.09489.
15 X. Zhu, and Q. Zhou, Flow structures of turbulent Rayleigh-Bénard convection in annular cells with aspect ratio one and larger, Acta Mech. Sin. **37**, 1291 (2021).
16 D. Wang, Z. Wang, S. Liu, L. Jiang, L. Yi, and C. Sun, Effects of complicated boundaries and extreme conditions on the flow structure and transport of single- and multi-phase turbulence. J. Tsinghua Univ. (Sci. Technol.) **62**, 758 (2022).
17 H. Jiang, X. Zhu, D. Wang, S. G. Huisman, and C. Sun, Supergravitational turbulent thermal convection, Sci. Adv. **6**, eabb8676 (2020), arXiv: 2010.07189.
18 A. Rouhi, D. Lohse, I. Marusic, C. Sun, and D. Chung, Coriolis effect on centrifugal buoyancy-driven convection in a thin cylindrical shell, J. Fluid Mech. **910**, A32 (2021).
19 D. Wang, H. Jiang, S. Liu, X. Zhu, and C. Sun, Effects of radius ratio on annular centrifugal Rayleigh-Bénard convection, J. Fluid Mech. **930**, A19 (2022).
20 D. Wang, S. Liu, Q. Zhou, and C. Sun, Spectra and structure functions of the temperature and velocity fields in supergravitational thermal turbulence, Phys. Fluids **34**, 055108 (2022).
21 H. Jiang, D. Wang, S. Liu, and C. Sun, Experimental evidence for the existence of the ultimate regime in rapidly rotating turbulent thermal convection, Phys. Rev. Lett. **129**, 204502 (2020), arXiv: 2110.01224.
22 D. Wang, J. Liu, Q. Zhou, and C. Sun, Statistics of temperature and velocity fluctuations in supergravitational convective turbulence, Acta Mech. Sin. **39**, 122387 (2023).
23 M. Heimpel, J. Aurnou, and J. Wicht, Simulation of equatorial and high-latitude jets on Jupiter in a deep convection model, Nature **438**, 193 (2005).
24 P. L. Read, Y. H. Yamazaki, S. R. Lewis, P. D. Williams, K. Miki-Yamazaki, J. Sommeria, H. Didelle, and A. Fincham, Jupiter's and Saturn's convectively driven banded jets in the laboratory, Geophys. Res. Lett. **31**, L22701 (2004).
25 P. B. Rhines, Waves and turbulence on a beta-plane, J. Fluid Mech. **69**, 417 (1975).
26 Y. Wang, X. He, and P. Tong, Turbulent temperature fluctuations in a closed Rayleigh-Bénard convection cell, J. Fluid Mech. **874**, 263 (2019).
27 Y. Wang, Y. Wei, P. Tong, and X. He, Collective effect of thermal plumes on temperature fluctuations in a closed Rayleigh-Bénard convection cell, J. Fluid Mech. **934**, A13 (2022).
28 Y. Bao, J. Chen, B. F. Liu, Z. S. She, J. Zhang, and Q. Zhou, Enhanced heat transport in partitioned thermal convection, J. Fluid Mech. **784**, R5 (2015).
29 Y. Bao, Z. P. Lin, and P. He, Influence of *Ra* number on flow and heat transfer in partitioned Rayleigh-Bénard convection, Sci. Sin.-Phys. Mech. Astron. **49**, 044701 (2019).
30 J. Chen, Y. Bao, Z. X. Yin, and Z. S. She, Theoretical and numerical study of enhanced heat transfer in partitioned thermal convection, Int. J. Heat Mass Transfer **115**, 556 (2017).
31 X. Chen, D. P. Wang, and H. D. Xi, Reduced flow reversals in turbulent convection in the absence of corner vortices, J. Fluid Mech. **891**, R5 (2020).
32 S. Ciliberto, S. Cioni, and C. Laroche, Large-scale flow properties of turbulent thermal convection, Phys. Rev. E **54**, R5901 (1996).
33 K. Q. Xia, and S. L. Lui, Turbulent thermal convection with an obstructed sidewall, Phys. Rev. Lett. **79**, 5006 (1997).
34 X. He, Y. Wang, and P. Tong, Dynamic heterogeneity and conditional statistics of non-Gaussian temperature fluctuations in turbulent thermal convection, Phys. Rev. Fluids **3**, 052401 (2018).
35 X. L. Qiu, and P. Tong, Large-scale velocity structures in turbulent thermal convection, Phys. Rev. E **64**, 036304 (2001).
36 H. Jiang, X. Zhu, V. Mathai, R. Verzicco, D. Lohse, and C. Sun, Controlling heat transport and flow structures in thermal turbulence using ratchet surfaces, Phys. Rev. Lett. **120**, 044501 (2018), arXiv: 1712.09303.
37 S. Grossmann, and D. Lohse, Multiple scaling in the ultimate regime of thermal convection, Phys. Fluids **23**, 045108 (2011).
38 R. H. Kraichnan, Turbulent thermal convection at arbitrary prandtl number, Phys. Fluids **5**, 1374 (1962).
39 P. E. Roche, The ultimate state of convection: A unifying picture of very high Rayleigh numbers experiments, New J. Phys. **22**, 073056 (2020).
40 E. A. Spiegel, Convection in stars I. Basic boussinesq convection, Annu. Rev. Astron. Astrophys. **9**, 323 (1971).

隔板超重力热湍流中的温度脉动和热输运

王东璞, 刘婧, 赖茹诗, 孙超

摘要 本文报道了隔板超重力湍流对流系统中的局部温度波动δT和热输运的实验研究. 在没有隔板的正常系统中, 由于纬向流流动的动力学, 混合区中某位置的概率密度函数(PDF)呈现向下弯曲的形状, 表明多羽流聚集效应起着重要作用. 在隔板系统中, 纬向流受到抑制, PDF表明单羽流效应占主导地位. 此外, 统计分析表明, δT的PDF对超重力是敏感的. 此外, 在正常系统中, 热能谱遵循$P(f) \sim f^{-5}$, 这与纬向流有关. 在隔板系统中, $P(f)$的标度指数的绝对值和标度范围变小, 这为纬向流对能量级串的影响提供了另一个证据. 此外, 在隔板系统中发现了传热增强, 这可能是由于纬向流受限, 进而促进了羽流向对侧导热圆柱的径向运动. 这项工作为理解一些工程和地球物理流提供了思路.